Axisymmetric draining of a cylindrical tank with a free surface

By QIAO-NIAN ZHOU AND W. P. GRAEBEL

Department of Mechanical Engineering and Applied Mechanics, The University of Michigan,
Ann Arbor, MI 48109, USA

The withdrawal of layered fluids from an open tank through a hole centred on the bottom is investigated numerically under the assumption of potential flow. A fully cubic-spline nonlinear axisymmetric boundary-integral-method scheme with the built-in boundary conditions, which effectively reduces the numerical errors at the intersection lines where the tank wall and the density interfaces meet, is used. Two cases are studied: (i) the tank contains only one fluid with a free surface; (ii) the tank contains two fluids having different densities with a distinct interface and a free surface.

The numerical results show two different phenomena, depending upon the drain rate and initial conditions. When the tank is rapidly drained, a dip forms at the centre of the lower interface and extends into the hole very quickly, as observed by Lubin & Springer (1967). For a slowly draining tank, a jet forms in the centre of the depression region. This jet can either shoot up or move down, depending on the initial conditions.

1. Introduction

When a fluid is withdrawn from an open circular tank through a finite sink located at the centre of the bottom, sudden formation of a dip is often observed in the centre of the free surface. The axisymmetric withdrawal of both one- and two-layer fluids from a circular tank has been studied experimentally and analytically by Lubin & Springer (1967), who found a relation between the critical height, the drain rate and the density ratio. They observed that the drain rate is nearly constant throughout the draining process until a dip is formed. The formation of the dip is so quick that it appears to extend into the sink almost instantly. The analytic formula obtained by Lubin & Springer is in excellent agreement with their experimental data, in spite of the fact that only the Froude number based on the drain rate, which is assumed a constant, and the density ratio are included. Their analytic solution is the limit for large initial depth of the lower surface and small sink.

The purpose of the present paper is to study the axisymmetrical evolution of a free surface and an interface in a circular tank under a constant drainage rate. The emphasis is on the transient surface configurations when the mean depth of the lower surface, which is the interface in a two-layer fluids system or the free surface in a one-layer fluid system, becomes small, and nonlinear effects are strong. We show an unexpected phenomenon: for small drain rate, a jet appears in the centre of the depression region in the centre of the lower surface owing to the off-centre surface particles squeezing those fluid particles near the centre of the lower surface.

It is also of interest to examine the effects of factors such as the size of the sink, the initial depths of the layers of fluids, etc. on the subsequent motion. It is
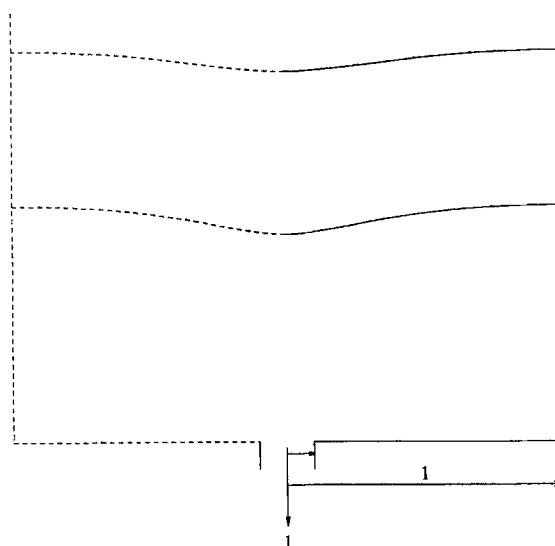
FIGURE 1. Two-dimensional dimensionless flow configuration (front view of the tank).

conceivable that those factors may modify considerably, or even completely change, the surface configurations. Zhou (1989) studied this problem numerically and found for the one-layer-fluid case that when a dip forms, the computed critical heights agree with Lubin & Springer's analytic solution only for moderate values of the Froude number. For large Froude numbers the computed values are considerably smaller than their analytic values. The discrepancies increase with the Froude numbers, and vary with the sink sizes and the initial depths of the free surface. For the two-layer-fluid case the differences are even larger. It was also found that there are strong free-surface oscillations as predicted theoretically by Saad & Oliver (1964) and Zhou & Graebel (1989).

For the present problem, the primary quantities of interest are the surface values such as the locations of the surfaces, surface velocities, etc. The boundary integral method (BIM) is a very efficient numerical method for such problems. Axisymmetric BIM schemes have been developed and applied by a number of researchers, including Baker, Meiron & Orszag (1984) and Dommermuth & Yue (1987). In this article we use a nonlinear axisymmetric BIM scheme similar to that of Dommermuth & Yue (1987), with the important modification that in the present model, both the velocity potential and the normal velocity on the boundary are represented by cubic splines with built-in boundary conditions which ensure a high order of smoothness of the solution. This scheme greatly reduces numerical errors at the point where the free surface or interface intersect the wall.

2. Mathematical formulation

We consider axisymmetric flows of both one or two layers of fluids in a circular tank. The lower fluid is withdrawn from the tank through a hole with finite radius placed in the centre of the tank bottom. Both fluids are assumed to be inviscid and incompressible. The top surface is taken as a free surface. On both the free surface and the interface, surface tension is neglected. Since the aim of the present research is to investigate the unsteady nonlinear motions of the free surface and interface

under drainage, we require that the upper fluid be lighter than the lower one, so that the stratification is stable. The drain rate is taken to be a constant, Q, and the flow is started in a discontinuous manner. It is expected that an impulsive start of surface motions would give the maximum surface distortion (Zhou & Graebel 1989).

We choose the radius R of the tank as the characteristic length, $T = R^3/Q$ as the characteristic time and $U = Q/R^2$ as the characteristic velocity. The potential is scaled by Q/R. In dimensionless units, the radius of the tank is thus unity. The dimensionless sink radius is a.

Let subscripts l and u denote the quantities pertinent to the lower and the upper fluid, respectively. With all quantities in their respective non-dimensional forms, the velocity potentials satisfy the Laplace equation

$$\nabla^2 \phi_j = 0 \quad ((r, z) \in \omega_j), \tag{1}$$

where $j = \ell, \mathrm{u}$; ω_ℓ and ω_u are the volumes as shown in figure 1. The boundary conditions on the tank wall are

$$\frac{\partial \phi_j(1, z, t)}{\partial r} = 0 \quad (j = \ell, \mathrm{u}), \tag{2}$$

$$\frac{\partial \phi(r, 0, t)}{\partial z} = \begin{cases} -v_0(r) & (0 \leqslant r \leqslant a), \\ 0 & (a \leqslant r \leqslant 1), \end{cases} \tag{3}$$

where $v_0(r)$ is the normal velocity distribution at the drain. The choice of the function $v_0(r)$ is restricted by global volume conservation, which requires that

$$2\pi \int_0^a v_0(r)\, r\, \mathrm{d}r = 1. \tag{4}$$

Obviously, the choice of defining $v_0(r)$ is not unique. The criterion adopted in this paper is that v_0 should not degenerate the overall accuracy and the smoothness of the solution. To be compatible with the cubic-spline approximation, we use

$$v_0(r) = \frac{10}{3\pi a^2}\left(1 + 2\frac{r}{a}\right)\left(1 - \frac{r}{a}\right)^2 \quad (0 \leqslant r \leqslant a). \tag{5}$$

Pressure can be obtained from the Bernoulli equation

$$p = -\bar{\rho}_j\left(\frac{\partial \phi_j}{\partial t} + \tfrac{1}{2}|\nabla\phi_j|^2 + F^{-2}z\right) \quad ((r, z) \in \omega_j, \quad j = \ell, \mathrm{u}), \tag{6}$$

where $\bar{\rho}_j = \rho_j/\rho_\ell$ so that $\bar{\rho}_\ell = 1$ and $\bar{\rho}_\mathrm{u} = \beta$ with $\beta = \rho_\mathrm{u}/\rho_\ell$. For a statically stable stratification, $\beta < 1$. Setting $p = 0$ in (6), we obtain the dynamic boundary condition on the free surface γ_f

$$\frac{\partial \phi_\mathrm{u}}{\partial t} + \tfrac{1}{2}|\nabla\phi_\mathrm{u}|^2 + F^{-2}z = 0 \quad ((r, z) \in \gamma_\mathrm{f}). \tag{7}$$

Because surface tension and viscosity are neglected, the dynamic condition on the interface is that the pressure on both sides of the interface γ_i be equal. Thus at the interface we require that

$$\frac{\partial \phi_\ell}{\partial t} + \tfrac{1}{2}|\nabla\phi_\ell|^2 - \beta\left(\frac{\partial \phi_\mathrm{u}}{\partial t} + \tfrac{1}{2}|\nabla\phi_\mathrm{u}|^2\right) + (1 - \beta)F^{-2}z = 0 \quad ((r, z) \in \gamma_\mathrm{i}). \tag{8}$$

In the above, F is the Froude number defined by

$$F = \frac{Q}{R^2(gR)^{\frac{1}{2}}}. \tag{9}$$

The kinematic condition on the interface is that particles of the upper fluid cannot penetrate into the lower fluid, and *vice versa*. This means that the velocity components normal to the interface cannot be discontinuous, and hence

$$\boldsymbol{n} \cdot \boldsymbol{\nabla}(\phi_{\mathrm{u}} - \phi_{\ell}) = 0 \quad ((r, z) \in \gamma_{\mathrm{i}}), \tag{10}$$

where $\boldsymbol{n}$ denotes the unit vector normal to γ_{i}.

The material points of the free surface are chosen as the Lagrangian points which represent the free surface. The position vector of the free-surface Lagrangian marker, denoted as s_{f}, satisfies

$$\frac{\partial \boldsymbol{x}_{\mathrm{f}}(s_{\mathrm{f}}, t)}{\partial t} = \boldsymbol{\nabla}\phi_{\mathrm{u}}(s_{\mathrm{f}}, t). \tag{11}$$

The choice of the interfacial Lagrangian points is somewhat arbitrary. Here we take the velocity of the Lagrangian markers, denoted by s_{i}, to be a weighted average of the upper and lower velocities at the interface. Thus

$$\frac{\partial \boldsymbol{x}_{\mathrm{i}}(s_{\mathrm{i}}, t)}{\partial t} = \boldsymbol{v}_{\mathrm{i}}(s_{\mathrm{i}}, t), \tag{12}$$

in which $\boldsymbol{x}_{\mathrm{i}}(s_{\mathrm{i}}, t)$ is the position of the interfacial Lagrangian point and $\boldsymbol{v}_{\mathrm{i}}(s_{\mathrm{i}}, t)$ is defined by

$$\boldsymbol{v}_{\mathrm{i}}(s_{\mathrm{i}}, t) = \alpha\boldsymbol{\nabla}\phi_{\ell} + (1-\alpha)\boldsymbol{\nabla}\phi_{\mathrm{u}}, \tag{13}$$

with $0 \leqslant \alpha \leqslant 1$. If α is taken as either one or zero, the interfacial Lagrangian marker will follow a material point of either the lower or upper fluid on the interface. Both $\alpha = 0.5$ and 1 were tried, and only slight differences in the surface shape were found. The numerical results reported in this paper are obtained using $\alpha = 1$.

According to (7), the potential that follows a Lagrangian point on the free surface is advanced in time by

$$\frac{\partial \phi_{\mathrm{u}}(s_{\mathrm{f}}, t)}{\partial t} = \tfrac{1}{2}|\boldsymbol{\nabla}\phi_{\mathrm{u}}|^2 - F^{-2}z_{\mathrm{f}}(s_{\mathrm{f}}, t), \tag{14}$$

in which $z_{\mathrm{f}}(s_{\mathrm{f}}, t)$ is the z-coordinate of the Lagrangian point s_{f}.

Define

$$\mu(s_{\mathrm{i}}, t) = \phi_{\ell}(s_{\mathrm{i}}, t) - \beta\phi_{\mathrm{u}}(s_{\mathrm{i}}, t), \tag{15}$$

where, if $\beta = 1$, μ is the conventional dipole strength. With the velocity of the interfacial Lagrangian point given by (13), the evolution equation for the interfacial potential is

$$\frac{\partial \mu(s_{\mathrm{i}}, t)}{\partial t} = \boldsymbol{v}_{\mathrm{i}} \cdot \boldsymbol{\nabla}\mu + \tfrac{1}{2}(\beta|\boldsymbol{\nabla}\phi_{\mathrm{u}}|^2 - |\boldsymbol{\nabla}\phi_{\ell}|^2) - (1-\beta)F^{-2}z_{\mathrm{i}}(s_{\mathrm{i}}, t), \tag{16}$$

in which $z_{\mathrm{i}}(s_{\mathrm{i}}, t)$ is the z-coordinate of the Lagrangian point s_{i}.

Since the flow is started impulsively, the initial conditions are

$$\phi_{\mathrm{u}}(s_{\mathrm{f}}, 0) = 0, \quad \mu(s_{\mathrm{i}}, 0) = 0. \tag{17}$$

The equations governing a one-layer fluid tank are readily obtained from the above.

3. Numerical implementation

Let $\partial\omega_\ell$ and $\partial\omega_u$ be the boundary curves of ω_ℓ and ω_u, respectively, but without the segments on the centreline, i.e. $\partial\omega_\ell = \gamma_i + B_\ell(t) + B_0$, $\partial\omega_u = \gamma_i + \gamma_f + B_u(t)$ as shown in figure 1.

By virtue of Green's theorem, we can write the general solution of (1) in the form

$$\alpha_j(r, z, t)\,\phi_j(r, z, t) = \int_{\partial\omega_j} \left[\frac{\partial\phi_j}{\partial n} G_j(r, z; r_s, z_s) - \phi_j \frac{\partial G_j(r, z; r_s, z_s)}{\partial n}\right] r_s \, dl_s \quad ((r, z) \in \omega_j), \quad (18)$$

in which

$$\alpha_j(r, z, t) = \begin{cases} 4\pi, & \text{when } (r, z) \in \omega_j, \\ 2\pi, & \text{when } (r, z) \text{ is a regular node,} \\ \pi, & \text{when } (r, z) \text{ is an intersection point.} \end{cases} \quad (19)$$

Here the contact angle between the surfaces and the wall is $\frac{1}{2}\pi$ (see Appendix). Also

$$G_u(r, z; r_s, z_s) = \int_0^{2\pi} \frac{d\theta}{(r^2 + r_s^2 - 2rr_s\cos\theta + (z - z_s)^2)^{\frac{1}{2}}} = \frac{4K(2b/c)}{c^{\frac{1}{2}}}, \quad (20a)$$

and

$$G_\ell(r, z; r_s, z_s) = G_u(r, z; r_s, z_s) + G_u(r, z; r_s, -z_s), \quad (20b)$$

where K is the complete elliptical integral of the second kind, and $b = 2rr_s$, $c = (r + r_s)^2 + (z - z_s)^2$. The image term in $G_\ell(r, z; r_s, z_s)$ is introduced to make $\partial G_\ell(r, 0; r_s, z_s)/\partial z = 0$. Therefore, the integral $\int_{B_0} \phi_\ell(\partial G_\ell/\partial n) r_s \, dl_s$ in (18) is eliminated. This yields a substantial numerical advantage by reducing the size of the resulting algebraic equation, and also by increasing the accuracy of the numerical solution, since ϕ_ℓ takes very large values in the sink region $(0 \leqslant r \leqslant a)$.

3.1. *Boundary integral equation solutions*

To discretize (18), the boundary curves γ_i, γ_f, $B_\ell(t)$ and $B_u(t)$ are each divided into a number of small elements such that the intersection points where the tank wall and the interface or the free surface meet, are the end points of the elements. On each boundary curve the solutions ϕ and $\partial\phi/\partial n$ are approximated by cubic splines. Then, (18) is collocated at nodes which are the end points of the elements. There is no need to discretize the tank bottom B_0 since $\partial\phi_\ell/\partial n$ on B_0 is known by virtue of (3) and (5).

Special care is taken at the intersection points, where the slopes are discontinuous, to avoid large numerical errors. A brief description of the difficulties near such intersection points is given by Dommermuth & Yue (1987). For two-dimensional problems, Lin (1984) developed an approach in which both the stream and the potential functions at the intersection point are specified in the Cauchy integral equation. Dommermuth & Yue (1987) applied the same idea to axisymmetric flow problems. In essence, their idea postulates that the potential at the intersection point is continuous.

For the present problem, we adopt a similar postulate; that the potential is non-singular at the intersection of the wall with either the interface or the free surface. Furthermore, we postulate that the velocity is continuous at the intersection points. We assume that both the overall and the local accuracy near the intersection points can be improved by imposing the continuity of the velocity at the intersection points as well as at the centre of the surfaces. It is worth noting that a linear interpolation

of potential cannot have the velocity continuous at the centre and the intersection points without auxiliary compatibility conditions. With the above postulations and with the contact angle between a surface (either an interface or a free surface) and the wall a right-angle when surface tension is neglected, we specify the boundary conditions for the cubic splines as follows: (a) owing to axisymmetry, at the centre of the interface or the free surface (where $r = 0$), and the slopes of the surface line is zero, the radial derivatives of the surface potentials and the radial derivatives of the normal velocities on the surface are zero; (b) at the intersection points, the radial derivatives of the surface potentials are zero, the radial derivatives of the surface normal velocities are zero, and the vertical velocity on the tank wall are equal to the surface normal velocities; (c) at the joining point between $B_f(t)$ and B_0 the vertical velocity is equal to zero. These boundary conditions are necessary and sufficient to uniquely determine the cubic splines. The cubic-spline solution satisfying the above specified boundary conditions is then C^1 continuous at the intersection points, where the slopes are discontinuous, and is C^2 continuous on the regular boundary, where the slopes are continuous.

A solution satisfying the above compatibility conditions can still exhibit larger than acceptable errors near the intersection points. These errors are caused by the local singular behaviour of the kernel functions $G_j(r, z; r_s, z_s)$ and $\partial G_j(r, z; r_s, z_s)/\partial n$. It can be shown that G_j is logarithmically singular, and that $\partial G_j/\partial n$ has both a pole and a logarithmic singularity where $(r, z) \sim (r_s, z_s)$. To ensure numerical accuracy, we desingularize the integrals by subtracting out the singular terms. The singular parts of the integrals then are calculated analytically. The remaining regular parts of the integrals are evaluated numerically, using Gaussian quadrature. Comparison with a test example having a known exact solution shows that this approach eliminates local errors near the intersection point (Zhou 1989).

In the present formulation the unknowns on the free surface are the normal velocities. At the interface the unknowns are ϕ_f, ϕ_u and the normal velocities. On the tank wall, the unknowns are the potentials. At the intersection point between the wall and the free surface, the unknown is the normal free-surface velocity, and the potential is considered known. At the intersection point where the interface and the wall meet, the unknowns are ϕ_f, ϕ_u and the interfacial normal velocity. The known quantity on the free surface is the potential, and on the interface μ is known.

For a two-layer fluid, the connection between the two equations resulting from (18) is provided by (10) and (15). Numerical integrations are performed by using an 8-point Gaussian quadrature scheme.

In all of our computational cases, the surface nodal distributions are initially equispaced. For the present problem, it was found convenient to equally reposition the nodes on $B_f(t)$ and $B_u(t)$ each time (18) is solved. Therefore, the nodes on the tank wall (except at the intersection points) are not necessarily Lagrangian points. Unlike nonlinear surface-wave-breaking cases (Longuet-Higgins & Cokelet 1976), the Lagrangian points become sparse near the centre where a depression appears owing to the quick development of the dip.

The method described above differs only in details from BIM used by others, but the details are significant. Dommermuth & Yue (1987) used cubic splines for the free surface and body shapes, but only linear functions for velocity potential ϕ and normal velocity ϕ_n on the boundary. Experience with a simple test problem (Zhou 1989), for which the exact solution is known and the free surface is flat, has shown that linear interpolation for potential and its normal derivative on the boundary without auxiliary equations can produce intolerable local errors at the intersection

point where the type of boundary condition changes and the slope is discontinuous. The numerical solution does not converge to the exact one at the intersection point. Similar difficulties occur at the centre. The difficulties with the linear interpolation of ϕ and ϕ_n are that it cannot meet the compatibility conditions at the centre and the contact point, which are very important in the present problem. The use of cubic splines for velocity potential and normal velocity along with the cubic-spline approximation for boundary in the present method thus results in a substantial improvement in accuracy over the use of linear interpolations for boundary values of ϕ and ϕ_n. Furthermore, owing to the extremely large curvature in the centre of the free surfaces, we feel that cubic-spline approximations for ϕ and ϕ_n are necessary. The use of cubic splines as the interpolating functions also greatly reduces the number of nodes on the boundary, hence reducing the size of resulting matrix. Since the present scheme is a direct one, the time for solving the resulting algebraic equations is proportional to N^3, where N is the total number of the boundary nodes. Thus, fully cubic-spline solutions greatly reduce the computational cost.

Longuet-Higgins & Cokelet (1976) dealt with a two-dimensional problem in an infinite domain, hence did not have to contend with intersection points or vanishing Jacobians. They used Lagrange polynomials in a transformed domain. They encountered sawtooth instabilities which had to be removed by filtering. Such instabilities do not arise in the present work unless the time/or space steps were too large. Thus filtering was not necessary. Since their domains were infinite and the drains were not present, direct comparison is not possible.

3.2. *Time integration and numerical stability*

Knowing ϕ_u on the free surface and μ on the interface, (18) along with (9) and (15) can be solved for the normal velocities of both the surfaces and the interfacial values of ϕ_ℓ and ϕ_u. The surface tangential velocities can be obtained by differentiating the surface potentials, and $\nabla\phi_\ell$ and $\nabla\phi_u$ on both the surfaces can be computed. Then, (11), (12), (14) and (16) can be updated in time to find surface values for ϕ_u, μ and the locations of the surface Lagrangian points at the next time instance. The time integrations were performed using either a fourth-order Runge–Kutta scheme or a fourth-order Adam–Bashford–Moulton predictor–corrector scheme with the starting values computed by the fourth-order Runge–Kutta scheme. Both methods gave virtually the same results.

For the axisymmetric free-surface problems, Dommermuth & Yue (1987) gave a linear stability criterion for the fourth-order Runge–Kutta scheme which is equivalent to

$$\Delta t \leqslant F\left(\frac{8\Delta x}{\pi}\right)^{\frac{1}{2}}, \tag{21}$$

in which Δt is the timestep size and Δx is the local grid spacing. This criterion indicates that for the same grid spacing, timestep size must be reduced at smaller F values, to avoid temporal instability.

The inequality (21) is only a necessary, not a sufficient, condition for numerical stability. Therefore, it can only be considered as an upper bound for the timestep size Δt under a given local grid size Δx. For example, for the one-layer-fluid case when $F = 50$, $h_0 = 5$ and $a = 0.05$, sawtooth instability in the free-surface shape was found when 41 initially equal-spaced nodes are used to represent the free surface (which results in $\Delta x = 0.025$) and $\Delta t = 0.1$. This sawtooth instability disappears when Δt is reduced to 0.02. For this case, (21) gives the upper bound $\Delta t_{\max} = 12.6$.

In the present problem, the velocities near the centre of the interface in a two-layer fluid tank or the free surface in a one-layer fluid tank become large when the centre becomes close to the sink. These large velocities also cause numerical instability even when (18) is solved exactly. We adopt an approach similar to that used by Longuet-Higgins & Cokelet (1976) and later by Jansen (1986); that the timestep be such that the displacement of a surface material point be less than the minimum size of the surface grid spacing.

The accuracy of the numerical solution of (18) is checked by computing, at each time (18) is solved, the volume flux across the boundaries, given by

$$\Omega_j(t) = 2\pi \int_{\omega_j} \frac{\partial \phi_j}{\partial n} r_s \, dl_s \quad (j = \ell, u). \tag{22}$$

Here, Ω_j is evaluated by approximating $\partial \phi_j/\partial n$ by a cubic spline whose nodal values are found through solving (18), and then the integration is performed by Gaussian quadratures. From continuity considerations, we have $\Omega_\ell(t) = \Omega_u(t) = 0$.

The overall accuracy is further monitored by calculating, at each timestep, the mean levels of the interface and the free surface according to

$$h_i(t) = 2\pi \int_{\gamma_i} z_i \, r_s \, dl_s, \quad h_f(t) = 2\pi \int_{\gamma_f} z_f \, r_s \, dl_s. \tag{23}$$

Here, $h_i(t)$ and $h_f(t)$ are calculated by approximating z_i and z_f by cubic splines and then integrating analytically. Continuity considerations require that

$$E_f(t) = h_f(t) - \left(h_f(0) - \frac{t}{2\pi}\right) = 0, \quad E_i(t) = h_i(t) - \left(h_i(0) - \frac{t}{2\pi}\right) = 0, \tag{24}$$

where $h_f(0)$ and $h_i(0)$ are the initial mean depths of the free surface and the interface, respectively. Since the velocities will be large when the surface is near the sink, time integration can cause errors even though (18) is solved accurately. Thus $E_f(t)$, $E_i(t)$, $\Omega_\ell(t)$ and $\Omega_u(t)$ serve as monitors of the accuracy of the time integration. Our experiences indicate that (22) and (24) are reliable criterions for accuracy and stability although they are only necessary conditions.

4. Numerical results

4.1. *One-layer fluid with a free surface*

The non-dimensional parameters that determine the flow are the Froude number F defined by (9), the initial depth h_0 of the free surface and the radius a of the sink. The motion of the free surface strongly depends on these parameters. It is found that the free-surface configurations are nearly independent of h_0 when h_0 is larger than unity. This is due to the fact that the free surface remains nearly flat until the mean depth is small (less than unity). Our numerical computations found numerical instability when the time and spatial resolution were not sufficiently fine. This sawtooth type of instability can occur even when the mean height of the free surface is large (larger than unity) and the free surface is nearly flat. Once the numerical instability occurs it will not be damped unless artificial filtering or smoothing is applied. The growth rate of the sawtooth instability is small when the mean depth is larger than unity, and it increases rapidly when the mean depth becomes small and nonlinearity becomes dominant.
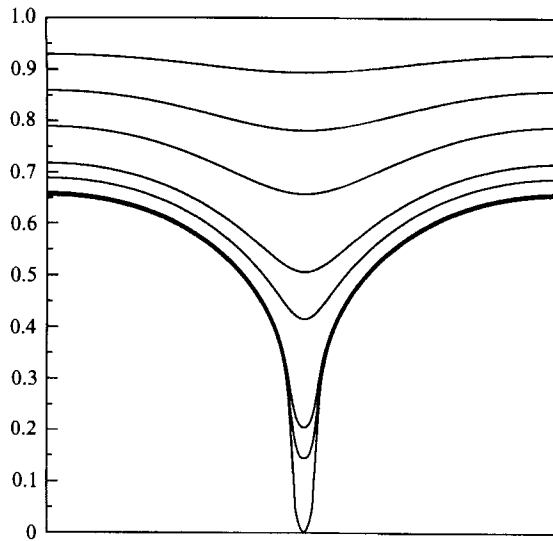
FIGURE 2. Time development of the free surfaces; $F = 1.0$, $h_0 = 1.0$, $a = 0.2$ at $t = 0.25$, 0.5, 0.75, 1.0, 1.1, 1.2, 1.21, 1.21975.
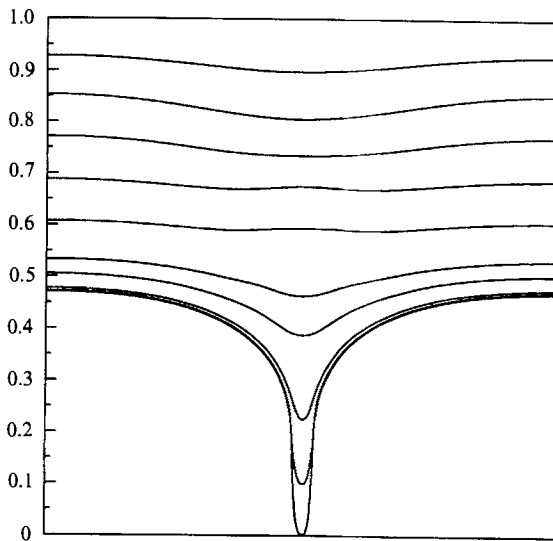

FIGURE 3. Time development of the free surfaces; $F = 0.5$, $h_0 = 1.0$, $a = 0.2$ at $t = 0.25$, 0.5, 0.75, 1.0, 1.25, 1.5, 1.6, 1.7, 1.72, 1.7248.

Figures 2 and 3 show the transient profiles of the free surface under different values of F but with the same initial height h_0 and drain radius a. They clearly show the sudden formation of a dip in the centre of the free surface. While no sign of the free-surface oscillation is seen in figure 2, it is clearly seen in figure 3. This indicates that a sufficiently large F (say larger than 1.0) can suppress the drainage-initiated free-surface oscillations as shown theoretically by Saad & Oliver (1964) and Zhou & Graebel (1989). The final configurations of the free surface in these two cases are similar despite the fact that they experience different motion histories. This suggests that when the mean level of the free surface is small, the sink influence dominates, and quickly damps out any existing oscillations.
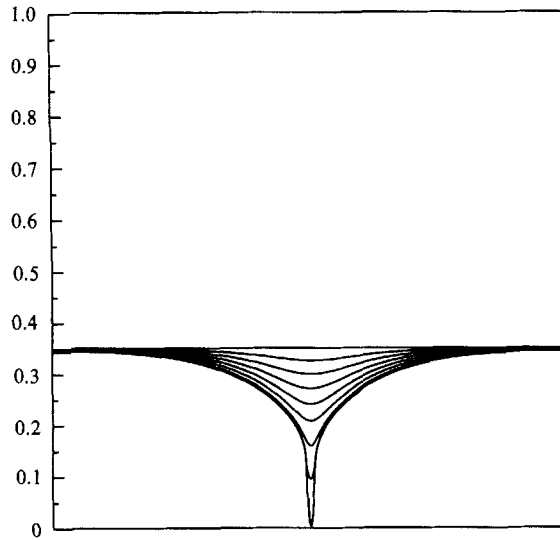
FIGURE 4. Time development of the free surfaces; $F = 0.1$, $h_0 = 0.35$, $a = 0.05$ at $t = 0$, 0.01, 0.02, 0.03, 0.04, 0.05, 0.06, 0.065, 0.06625.
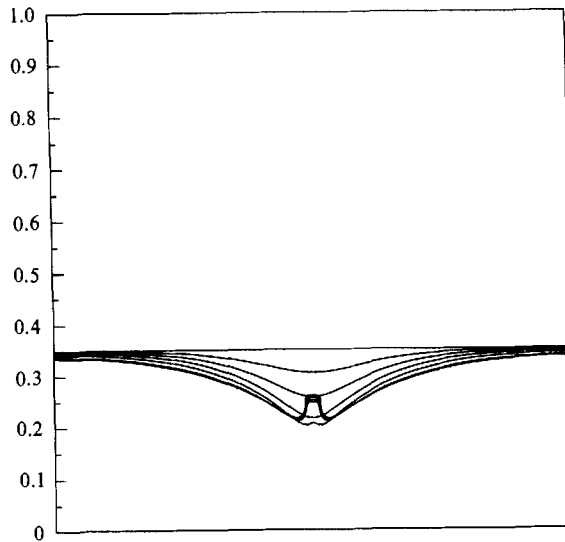
FIGURE 5. Time development of the free surfaces; $F = 0.1$, $h_0 = 0.35$, $a = 0.2$ at $t = 0$, 0.02, 0.04, 0.06, 0.08, 0.1, 0.102, 0.104, 0.106.

A rather surprising result is seen in figures 5 and 9. The difference between figures 4 and 5 is the radius of the sink. The radius a in figure 5 is four times as large as that in figure 4. This results in a maximum draw-down velocity occurring at the centre of the sink, which in figure 4 is sixteen times as large as that in figure 5. This implies that if F is sufficiently small, the draw-down provided by the sink is weak compared to gravity. The distances between surface points near the centre are compressed by the rest of the surface as shown in figure 8. Two totally different phenomena are thus possible depending on flow parameters: (i) a dip as shown in figure 4; (ii) a reverse jet as shown in figures 5 and 9. Since F and h_0 are the same in figures 4 and 5, a smaller a is seen to result in a greater draw-down of the free surface. Equivalently, one can
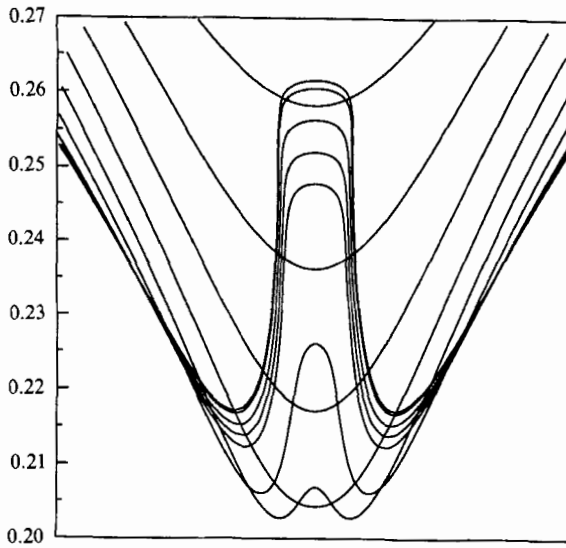
FIGURE 6. Close-up of the reverse jet region of figure 5. $0 \leqslant r \leqslant 0.2$ and $t = 0.04$, 0.05, 0.06, 0.07, 0.08, 0.09, 0.1, 0.102, 0.104, 0.106, 0.1065.
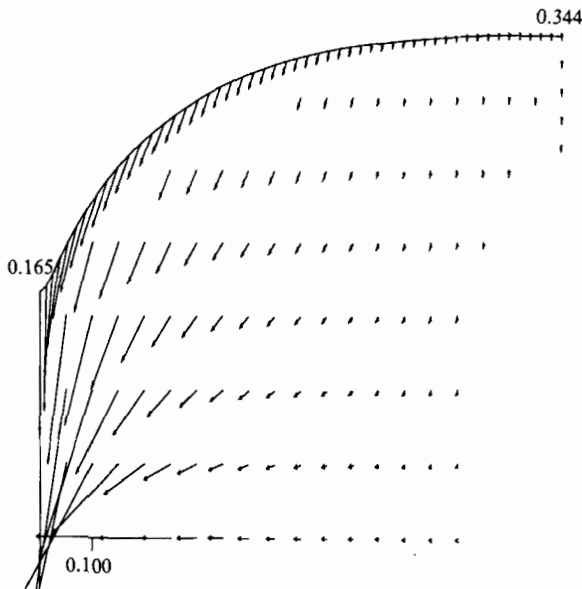

FIGURE 7. Velocity field when a dip forms; $F = 0.1$, $h_0 = 0.35$, $a = 0.1$ at $t = 0.064$.

say that a more concentrated draw-down force overcomes the squeezing of the near-centre surface points by the off-centre surface points, and a pulling down of the centre of the free surface. Thus a sufficiently small a can still give rise to a dip as demonstrated in figure 4. If a is not sufficiently small, the squeezing together of the near-centre surface points decelerates the centre. Consequently, it generates a reverse jet as shown in figures 5 and 9.

Figure 6 shows a close-up view of the jet. Figure 8 shows that the velocity of the surface is roughly of constant magnitude when the jet is well developed. How small a must be to ensure a dip depends on F as well as h_0. Figures 7 and 8 show the velocity

Q.-N. Zhou and W. P. Graebel
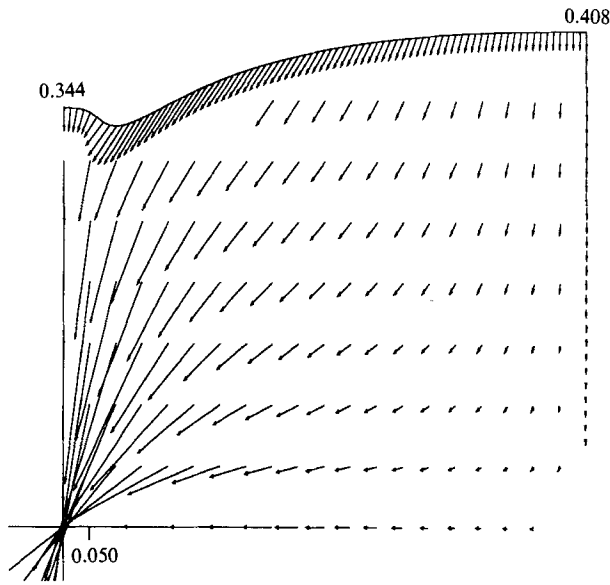
FIGURE 8. Velocity field when a reverse jet forms; $F = 0.25$, $h_0 = 1.0$, $a = 0.05$ at $t = 1.9$.
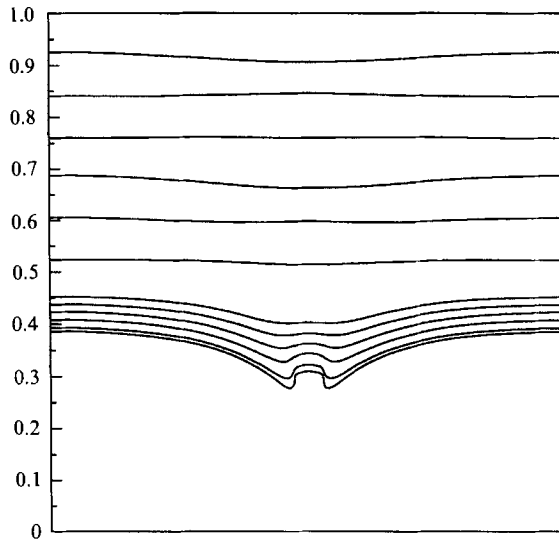

FIGURE 9. Time development of free surfaces; $F = 0.25$, $h_0 = 1.0$, $a = 0.05$ at $t = 0.25$, 0.5, 0.75, 1.0, 1.25, 1.5, 1.75, 1.8, 1.85, 1.9, 1.95, 1.973.

fields corresponding to the dip and the jet cases, respectively. Figure 7 shows that when a dip is about to form, the surface velocities near the centre are dominant while those away from the centre are small. This is the kinematic reason why the dip develops so rapidly as shown by Lubin & Springer (1967). Figure 8 shows that in the case where a reverse jet appears, the maximum surface velocity occurs at the trough of the free surface. If the trough velocity is sufficiently large, the centre must be pushed upward owing to the strong compression, hence a reverse jet will form.

  The effect of h_0 on whether a dip or a jet forms is similar to that of a. Figure 9 shows free-surface profiles which have the same parameters as those shown in figure 8. Figure 9 shows a weak jet whose tip moves down with the mean surface, while figure
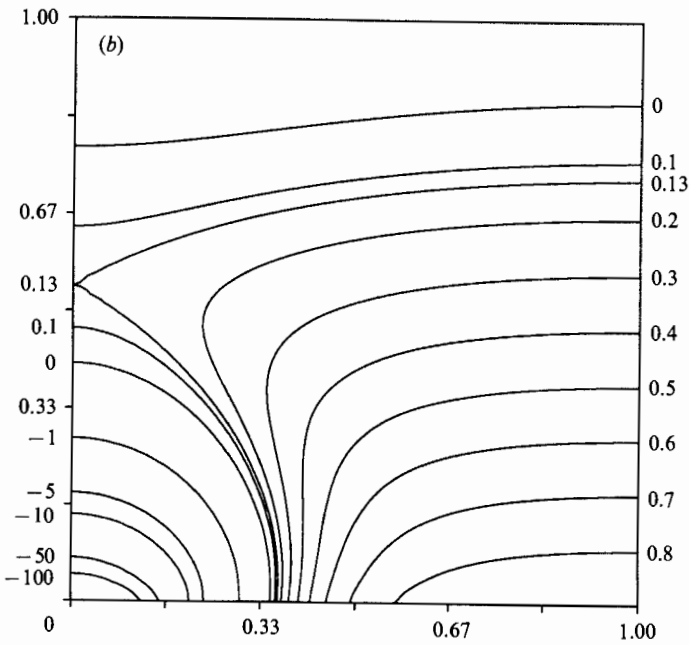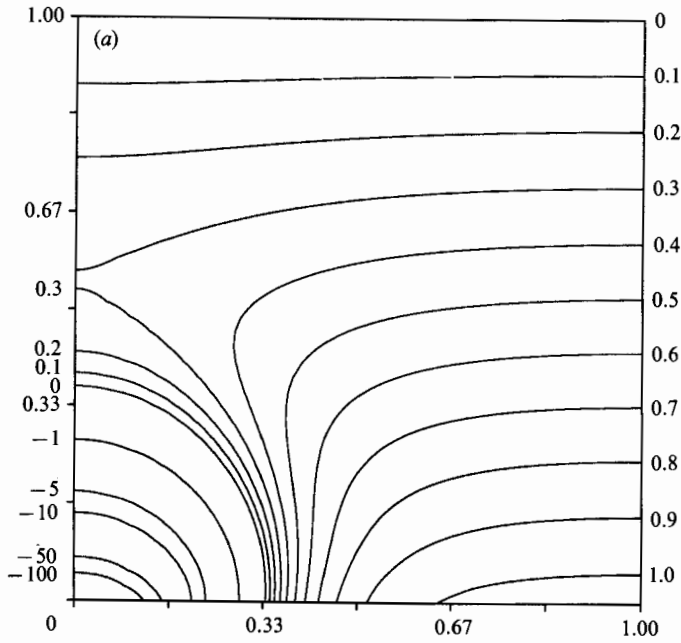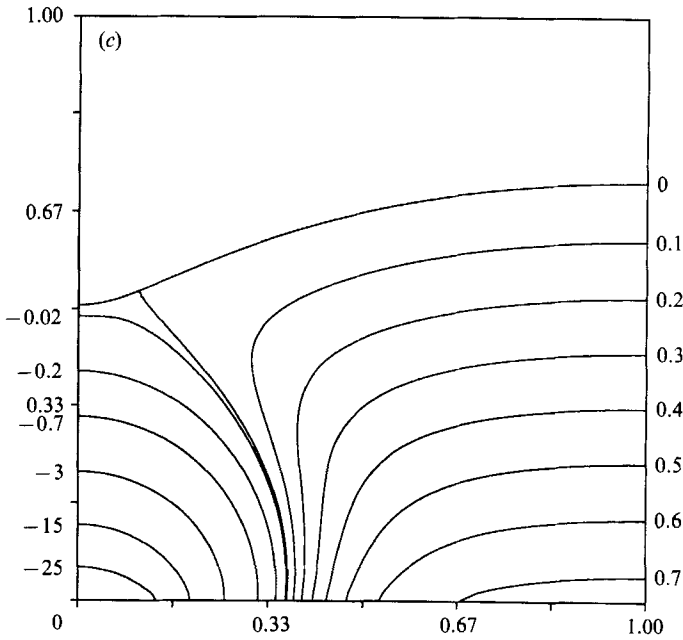
FIGURE 10 (*a*, *b*). For caption see page 524.

FIGURE 10. Contours of constant pressure (dip case); $F = 1.0$, $h_0 = 1.0$, $a = 0.2$.
(a) $t = 0$; (b) $t = 0.5$; (c) $t = 1.0$.

5 shows a strong jet which shoots upward. A weak jet occurs when the initial depth h_0 is large, and the drainage-initiated free-surface oscillations occur in the early stage of the motion. Comparing figure 7 with figure 8, we can see that the oscillations make the surface velocity distribution more uniform, hence the compression is weaker. This is possibly the reason why the jet in figure 9 moves down while the jet in figure 5 moves up.

We also calculated the vertical downward acceleration at the centre of the free surface. In all our calculations, we found that a dip appears only when the dimensionless downward acceleration exceeds F^{-2}, or equivalently when the dimensional downward acceleration exceeds the gravitational acceleration g. In the cases when a dip forms, the centre of the free surface first moves down at a nearly constant velocity, and then quickly transits to an exponentially accelerating motion when its acceleration is near F^{-2} (Zhou 1989). In cases where a jet occurs, this downward acceleration never exceeds F^{-2}. This suggests that the dip formation mechanism may be due to a local flow instability analogous to Rayleigh–Taylor instability (Taylor 1950), since the fictitious force induced by an accelerating fluid resembles a gravitational force. Supporting evidence may be found in a two-dimensional numerical simulation of Rayleigh–Taylor instability by Baker (1983). We can see that the dips shown in figures 2 and 3 qualitatively resemble the long spikes of the lower free surface as shown in figure 4 of Baker's paper, and both grow very rapidly. It is interesting that in Baker's simulation, a small reverse jet forms on the upper free surface.

In figures 10 and 11, constant pressure lines are shown at various times for a dip and a jet case, respectively. The top zero pressure line in each case is the free surface. In both cases, the pressure far away from the centreline is nearly hydrostatic with almost constant gradient, and there is a large pressure gradient near the sink which draws fluid into the sink. It is seen that besides the free-surface line, there is another
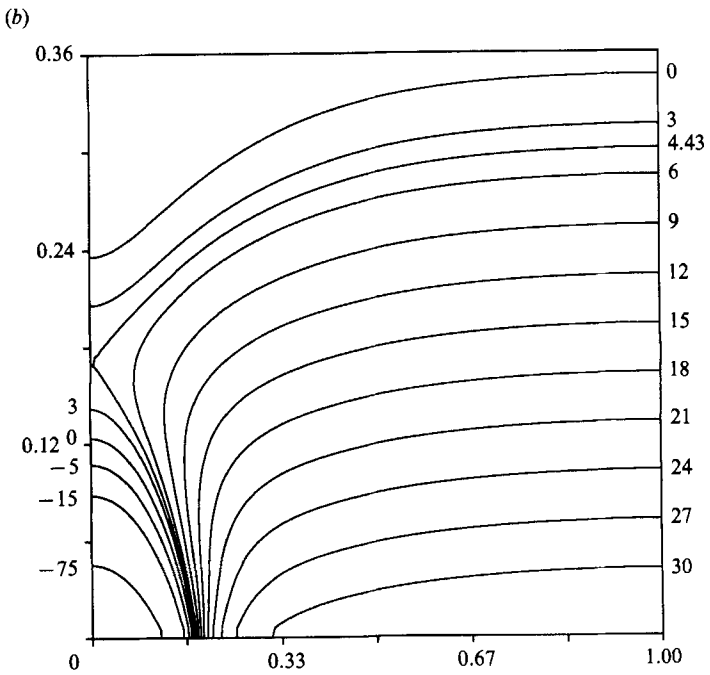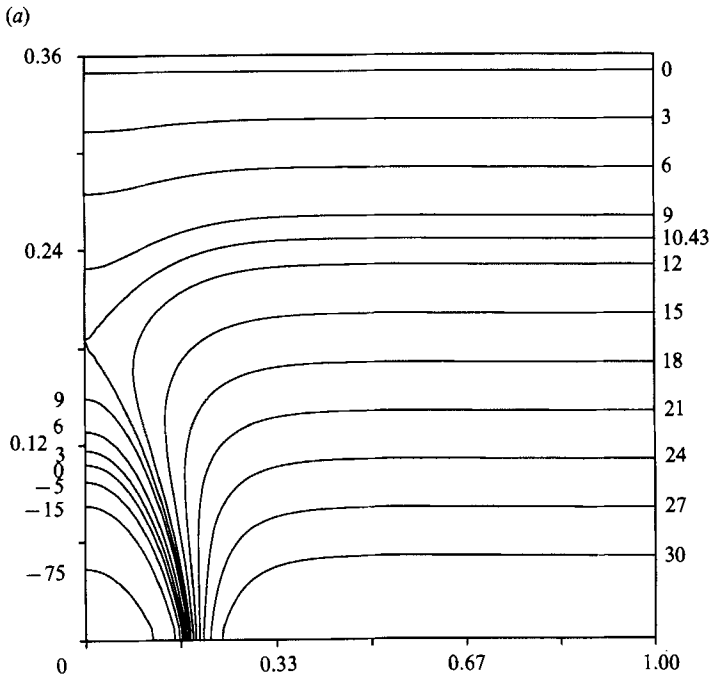
(a)

(b)

FIGURE 11 (a, b). For caption see page 526.

(c)
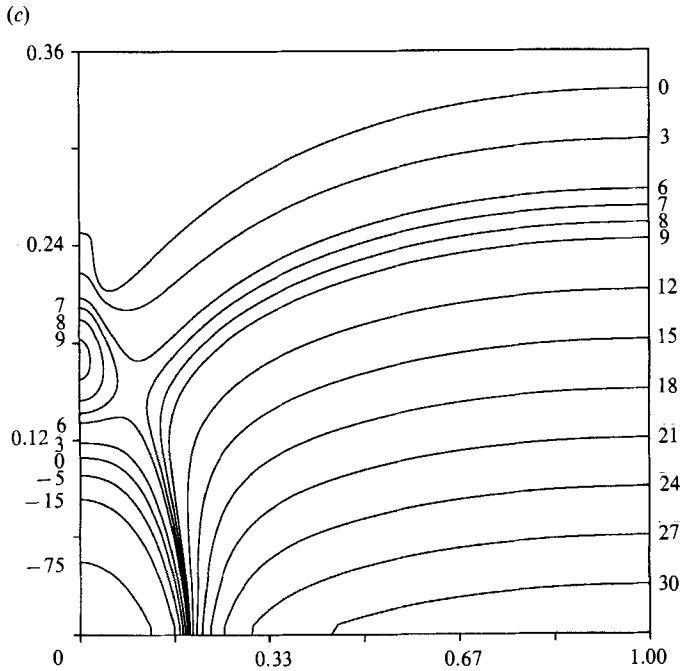

FIGURE 11. Contours of constant pressure (jet case); $F = 0.1$, $h_0 = 0.35$, $a = 0.2$.
(a) $t = 0$, (b) $t = 0.05$; (c) $t = 0.1$.

zero pressure line inside the flow region at early times when the dip or the jet has not formed. Figures 10 (a, b) and 11 (a, b) show that at early times, the patterns of constant pressure lines are similar for both cases. However, there are substantial differences in the pressure distribution at a later stage which result in the different phenomena.

For the dip case, figure 10 shows that a pressure distribution monotonically decreasing from the free surface develops on the centreline, and the internal zero pressure line merges with the free surface. The pressure gradient on the centreline is downward and draws down the centre of the free surface, hence a dip results. Figures 2 and 10 suggest that the starting time for the formation of the dip is that when the internal zero pressure line merges with the free surface. The merging of the two zero pressure lines is the necessary condition for the formation of a dip.

For the jet case, figure 11 shows that the two zero pressure lines cannot merge into one, and a local maximum pressure develops on the centreline. This is consistent with the jet. This type of local maximum pressure was previously observed by Baker *et al.* (1987) for a case of Rayleigh–Taylor instability. When the upward pressure gradient resulting from the local pressure high is weak, i.e. smaller than the gravitational force, the resulting jet will move down as shown in figure 9.

As described in §3.2, the accuracy in solving (18) was checked by computing the flux across the free surface. The error in the flux across the free surface remained at about 10^{-7} to 10^{-6} for most of the calculation, and increased to 10^{-5} at the end of the calculation when the tip region of the free surface started to develop very large curvatures. The overall accuracy is represented by the error in the mean level of the free surface. This error stayed at around 10^{-6} to 10^{-5}, increasing to 10^{-4} at the end of a calculation. At the end of a computation, when either the dip reaches the sink or curvatures became too extreme (in the case of jet formation), the surface curvature
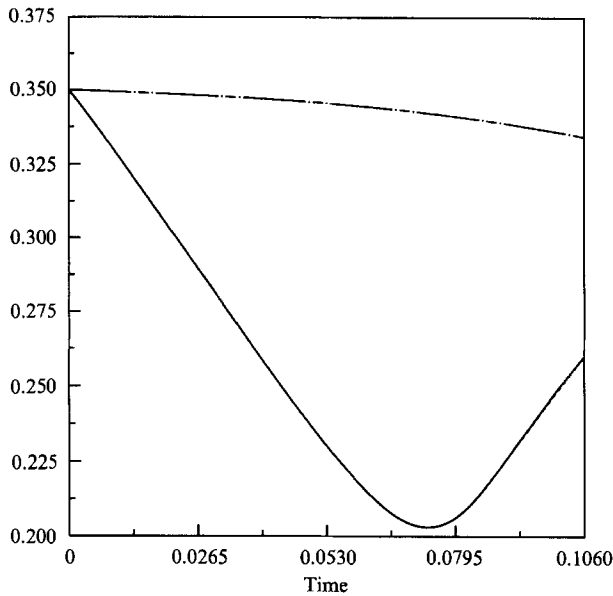
FIGURE 12. Comparison of z-coordinate of the centre ($r = 0$) (——, 41 nodes; – – –, 126 nodes) and the intersection point ($r = 1$) (— - — -, 41 nodes; ....., 126 nodes). $F = 0.1$, $h_0 = 0.35$, $a = 0.2$.

and the velocity near the centre of the free surface were very large. Extremely small timesteps and locally small boundary elements were needed. Our computer code broke down when the jet became well developed.

To test convergence, figure 12 compares trajectories of the centre ($r = 0$) and the intersection ($r = 1$) points of the free surface for the jet case using 41 and 126 initially equally spaced surface nodes, respectively. It is seen that convergence is excellent. The potentials for both runs at the centre at $t = 0.106$ is 1.2, and the difference is less than 0.04%.

4.2. *Two-layer fluid with both an interface and a free surface*

For the two-layer-fluid case, the parameters that govern the flow are the Froude number F, the sink radius a, the density ratio β and the initial depths h_ℓ and h_u of the lower and upper layers, respectively.

It should be noted that if $\beta = 1$, no vorticity can be created on the interface because viscosity and surface tension are neglected and the density is constant (Yih 1979, p. 63). Before the flow starts there is no flow, and thus no interfacial vorticity. This means that, when $\beta = 1$, the interface is no different to other material surfaces, and the interfacial dynamic condition (16) reduces to a trivial one. The flow thus reduces to the one-layer fluid flow described in §4.1. When $\beta \neq 1$, the sudden start of the flow creates an initial interfacial vorticity. This initial vortex strength distribution must be found by solving equation (18). In the same manner, there is an initial jump in the potential (dipole strength) across the interface.

In this section, we show results which illustrate how the two surfaces interact with each other. Figures 13 and 14 show two cases where F, a, h_ℓ and h_u are the same, but β is varied. Figure 13 shows the profiles of the interface and the free surface for a slightly stratified configuration ($\beta = 0.9$). It shows that when a dip forms on the interface, the free surface undergoes severe oscillations. Figure 14 shows the case of
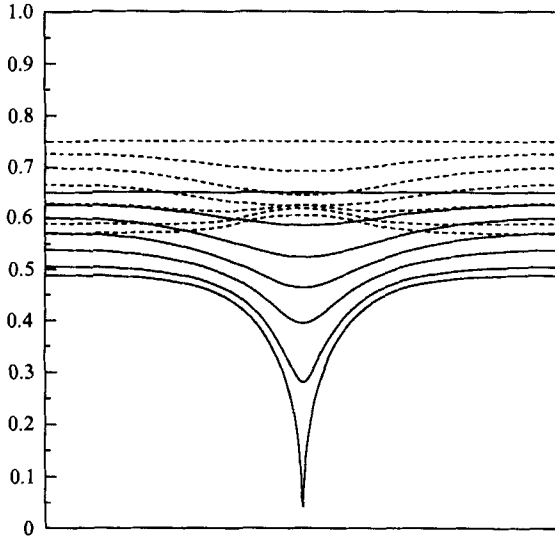
FIGURE 13. Time development of ----, the free surface and ———, the interface; $F = 0.25$, $a = 0.1$, $\beta = 0.9$, $h_\ell = 0.65$ and $h_u = 0.1$ at time $t = 0$, 0.1, 0.2, 0.3, 0.4, 0.5, 0.553.
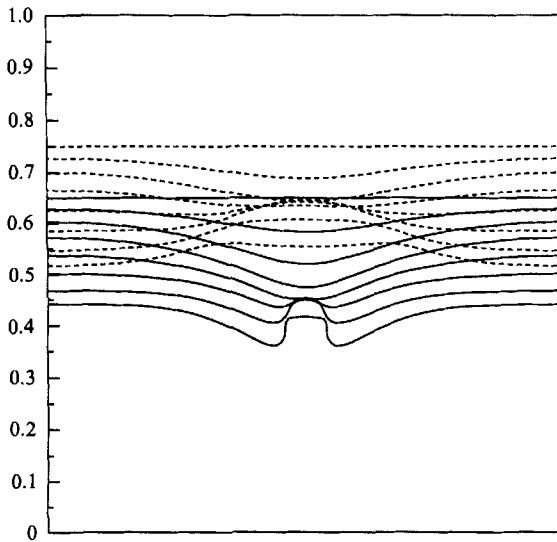

FIGURE 14. Time development of ----, the free surface and ———, the interface; $F = 0.25$, $a = 0.1$, $\beta = 0.5$, $h_\ell = 0.65$ and $h_u = 0.1$ at time $t = 0.3$, 0.5, 0.69.

a large stratification ($\beta = 0.5$). It clearly shows the sign of travelling waves on the free surface. In this case, a jet forms on the interface.

The physical mechanism as to why different values of β cause quite different surface motions can be explained by the interfacial vorticity. Figure 15 shows the interfacial vortex strength distribution corresponding to the two cases of figures 13 and 14. The vortex strength is the difference in the tangential velocities across the interface. When the vorticity is in the clockwise direction, it is positive. It can be seen that the interfacial vortex strength for large stratification ($\beta = 0.5$) is larger than that for small stratification ($\beta = 0.9$). This indicates that larger stratification induces
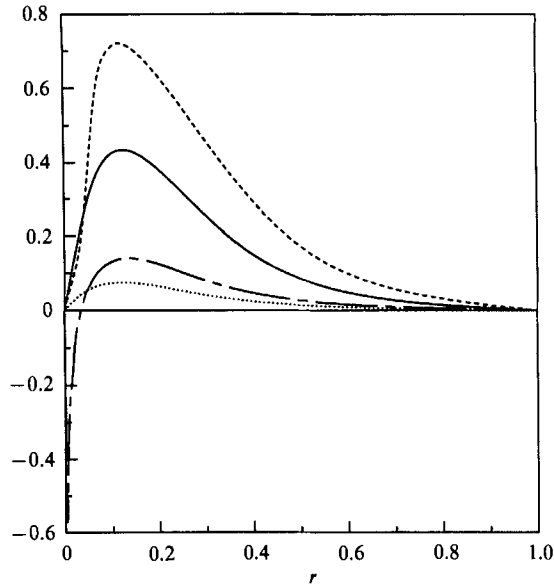
FIGURE 15. Time development of the interfacial vortex strength corresponding to the two cases shown in figures 13 and 14 where ——, $\beta = 0.5$, $t = 0.4$; ---, $\beta = 0.5$, $t = 0.55$; ·····, $\beta = 0.9$, $t = 0.4$; ————, $\beta = 0.9$, $t = 0.55$.

larger interfacial vortices. For the case $\beta = 0.5$, the maximum vortex strength appears at the trough of the interface. It is well known that a vortex sheet tends to roll up if there are no constraints. If we imagine a fictitious flow which possesses the same interfacial vortex distribution as that induced by the sink, but the flow is without a sink, owing to the roll-up the centre of the interface would go up to form a jet. However, the sink tends to pull down the centre of the interface. Whether a dip or a jet would occur is determined by whether the sink or roll-up is the dominant feature. If the sink is dominant, a dip will form as shown in figure 13. Otherwise, a jet appears as shown in figure 14. It can be seen that when a dip develops on the interface, the vortex strength near the centre is negative, which aids in pulling the centre of the interface into the sink. The negative vortex strength indicates that the inward (pointing towards the centreline) tangential velocity of the upper fluid on the interface is greater than that of the lower fluid on the interface. When a jet forms, the vortex strength is positive everywhere, indicating that particles of lower fluid on the interface move towards the centreline faster than do upper fluid particles on the interface.

It has been assumed in simple analytical analysis, e.g. Lubin & Springer (1967) and Harleman, Morgan & Purple (1959) that the pressure on an interface is approximately hydrostatic. Our numerical calculations found that this is correct only if the interfacial curvature is small (see Zhou 1989). When a dip develops on the interface, the pressure distribution also exhibits a dip in the centre of the interface. This pressure dip develops very quickly, as does the surface dip. Thus the assumption that the interfacial pressure is hydrostatic is no longer correct after an appreciable depression occurs on the interface.

5. Concluding remarks

A fully cubic-spline nonlinear BIM scheme has been developed to simulate the axisymmetric flow motion of a free surface and an interface inside a circular tank with a drain in the centre of the tank bottom. The BIM scheme is specially designed to ensure C^2 continuity on the regular boundary, and C^1 continuity at the contact points of the tank wall and the interfaces, where two different types of boundary conditions join together and there is no unique normal vector. A special treatment of the contact points, similar to the approaches used by Lin (1984) and Dommermuthy & Yue (1987), is extended to this high-order scheme. The high degree of smoothness of the numerical solution proves to be very effective in reducing the numerical errors, especially at the geometrically singular points and the confluence points. This numerical scheme could be extended to include surface tension with the adequate modification of the dynamic boundary conditions on the free surface and the interface, and with an evolution equation for the contact angle which, in the presence of surface tension, is no longer 90°.

The numerical results show that the drainage causes a depression in the centre of the lower surface, which is either the interface (two-layer) or the free surface (one-layer). The later configurations of the lower surface can be either a dip which extends into the sink, or a reverse jet. Whichever forms depends on all of the parameters in the problem. It is shown that for certain flow initial conditions, a reverse jet can form in the depression region. We suggest that the formation of the dip which extends into the sink is due to a type of flow instability analogous to Rayleigh–Taylor instability. This instability results in the subsequent catastrophic change in the surface shape, i.e. the quick extension of the dip into the sink.

The present BIM scheme results in a Fredholm equation of the first kind. The resulting algebraic equation has to be solved by direct matrix inversion, which is expensive and needs large amounts of computer storage. Iterative methods are more efficient and need less computer storage and time. We have also tried using a velocity formulation in order to formulate a Fredholm equation of the second kind which can be solved interactively. A vortex distribution on the interface and a source distribution on the tank wall were used. At the contact points, the vortex and the source strengths satisfy a compatibility equation which ensures that the velocities at the contact points are finite. The formulation was used to solve a test problem. The results showed that the numerical solution had large errors, especially at the contact point. Research on a formulation which would lead to the Fredholm equation of the second kind is of practical importance.

The present numerical scheme breaks down after a jet is well developed. It would be of physical interest to see the later stages of the evolution of the jet.

Appendix. The contact angle at the intersection points

Assuming that the fluid is inviscid and that surface tension is negligible, both surface and wall boundary conditions can be applied at the point where a material

surface intersects a wall. The velocity at that intersection point must be single valued. We show here that the contact angle between the wall and a material surface is 90°.

Suppose that $z_s(r, t)$ is an axisymmetric free surface. In the Lagrangian description, the momentum equation is

$$\frac{\partial V}{\partial t} = -\frac{1}{\rho} \nabla p - g e_z, \tag{A 1}$$

where $V(a, t) = u(a, t) e_r + w(a, t) e_z$ and e_r, e_z are the unit vectors in the directions of r- and z-axes respectively, and a is the Lagrangian identifier of the surface material point.

Let $s = s_r e_r + s_z e_z$ be the tangent vector at the surface, and take the inner product of s and (A 1). We have then

$$s_r \frac{\partial u}{\partial t} + s_z \frac{\partial w}{\partial t} = -\frac{1}{\rho} s \cdot \nabla p - g s_z. \tag{A 2}$$

Since surface tension is neglected, the pressure on the free surface is constant. Thus $s \cdot \nabla p = \partial p / \partial s = 0$ on the free surface. Applying (A 2) at the intersection point gives

$$s_z \left(\frac{\partial w}{\partial t} + g \right) = 0, \tag{A 3}$$

where we have assumed that at the wall $u = 0$, and consequently, $\partial u / \partial t = 0$.

Equation (A 3) suggests two possibilities. One is that

$$s_z = 0 \quad \text{at the intersection point.} \tag{A 4a}$$

The other is that

$$\frac{\partial w}{\partial t} + g = 0 \quad \text{at the intersection point.} \tag{A 4b}$$

Equation (A 4b) would be valid for free fall of the fluid. In this problem, the sink is much smaller than the cross-sectional area of the tank. Hence free-fall motion is impossible. The only case in which the fluid is in free-fall motion is when the sink covers the entire bottom of the tank. However, in the free-fall case, the free surface remains flat, and we still have $s_z = 0$. Hence the second possibility is ruled out. Equation (A 4b) means the free surface must contact the wall at 90°.

If the surface is an interface, the momentum equations are

$$\frac{\partial V_\ell}{\partial t} = -\frac{1}{\rho_\ell} \nabla p_\ell - g e_z, \quad \text{in the lower layer,} \tag{A 5}$$

and

$$\frac{\partial V_u}{\partial t} = -\frac{1}{\rho_u} \nabla p_u - g e_z, \quad \text{in the upper layer.} \tag{A 6}$$

Thus we have

$$s \cdot \left(\rho_\ell \frac{\partial V_\ell}{\partial t} - \rho_u \frac{\partial V_u}{\partial t} \right) = s \cdot \nabla (p_u - p_\ell) - (\rho_\ell - \rho_u) g s_z. \tag{A 7}$$

At the interface, $p_\ell = p_u$ since the fluid is free of viscosity and surface tension. Thus the pressure-difference term in (A 7) is zero. At the intersection point, the velocity of both layers should be single valued. Thus the radial velocity must be zero and the vertical velocity must be equal for both layers. Then

$$(\rho_\ell - \rho_u) s_z \left(\frac{\partial w}{\partial t} + g \right) = 0, \tag{A 8}$$

where $w = w_\ell = w_u$ is the common vertical velocity of both layers at the intersection point. We see that s_z must be zero by the same argument as before.

REFERENCES

BAKER, G. R. 1983 Generalized vortex method for free-surface flows. In *Waves on Fluid Interfaces* (ed. R. E. Meyer), p. 53. Academic.

BAKER, G. R., McCRORY, R. L., VERDON, C. P. & ORSZAG, S. A. 1987 Rayleigh–Taylor instability of fluid layers. *J. Fluid Mech.* **178**, 161.

BAKER, G. R., MEIRON, D. I. & ORSZAG, S. A. 1984 Boundary integral methods for axisymmetric and three-dimensional Rayleigh–Taylor instability problems. *Physica* **12D**, 19.

DOMMERMUTH, D. G. & YUE, D. K. 1987 Numerical simulation of nonlinear axisymmetric flows with a free surface. *J. Fluid Mech.* **178**, 195.

HARLEMAN, D. R. F., MORGAN, R. L. & PURPLE, R. A. 1959 Selective withdrawal from a vertically stratified fluid. *Intl Assoc. Hydraul. Res. Proc. 8th Congress*, vol. 2, paper 10-C.

JANSEN, P. C. M. 1986 A boundary element model for non-linear free surface phenomena. Delft University of Technology, Dept. of Civil Engng, Rep. no. 86-2.

LIN, W. M. 1984 Nonlinear motion of free surface near a moving body. PhD thesis, MIT, Dept. of Ocean Engng.

LONGUET-HIGGINS, M. S. & COKELET, E. D. 1976 The deformation of steep surface waves on water. I. A numerical method of computation. *Proc. R. Soc. Lond.* A **350**, 1.

LUBIN, B. T. & SPRINGER, G. S. 1967 The formation of a dip on the surface of a liquid draining from a tank. *J. Fluid Mech.* **29**, 385.

SAAD, M. A. & OLIVER, D. A. 1964 Linearized time dependent free surface flow in rectangular and cylindrical tanks. In *Proc. Heat Transfer and Fluid Mech. Inst.*, p. 81. Stanford University Press.

TAYLOR, G. I. 1950 The instability of liquid surfaces when accelerated in a direction perpendicular to their plane. I. *Proc. R. Soc. Lond.* A **201**, 192.

YIH, C. S. 1979 *Fluid Mechanics*. West River Press, 3530 West Huron River Drive, Ann Arbor, MI 48103, USA.

ZHOU, Q. N. 1989 Numerical simulation of nonlinear interaction of density interfaces with a drain. PhD thesis, Dept. of Mech. Engng and Appl. Mech. The University of Michigan, Ann Arbor.

ZHOU, Q. N. & GRAEBEL, W. P. 1989 Free-surface oscillations in a slowly draining tank (submitted for publication).